Scalability of Fatigue Analyses Using Explicit Solvers

Frank A. Leone* and Carlos G. Dávila†
NASA Langley Research Center, Hampton, Virginia, 23681

A cohesive fatigue law has been integrated into a constitutive material model compatible with an explicit finite element solver. The cohesive fatigue model response is based on engineering approximations of the endurance limit and the Goodman diagram. This approach can predict stress-life diagrams for crack initiation, the Paris law regime, and transient effects of crack initiation and stable tearing. Simplified cyclic loading is utilized so that the applied load (or displacement) corresponds to the peak load of a fatigue cycle. Loads are held constant during fatigue while damage develops with increasing solution increments. An automatically-calculated ratio of fatigue cycles per solution increment controls the rate of damage growth, ensuring that damage growth is modeled with a sufficient minimum number of increments and damage growth advances to an extant of interest within the explicit analysis step time. The compatibility with an explicit finite element solver enables the analysis of structures that are computationally intractable for implicit finite element solvers. Scalability studies are conducted for geometrically nonlinear problems involving fiber-reinforced composite structures that exhibit fatigue damage growth of interacting matrix cracks and delaminations.

I. Introduction

As part of the NASA Advanced Composites Project (ACP), a verification and validation framework was developed and applied to a set of progressive damage analysis (PDA) methods for fiber-reinforced composite materials [1], with the goals of increasing confidence in the computational tools and advancing the state-of-the-art through additional method improvements. One of the focus problems for ACP was a post-buckled stiffened panel, in which networks of interacting matrix cracks and delaminations developed. A variety of PDA methods were exercised, including both continuum and discrete damage mechanics methods, methods compatible with implicit and explicit finite element (FE) solvers, and methods developed for static and fatigue loading conditions. The CompDam material model [2] was one of the methods selected for evaluation and further development during ACP. At the onset of the project, the CompDam material model had no existing fatigue prediction capabilities, and the model was limited to application to the statically loaded validation problems, including seven-point bending [3] and single stringer compression [4] specimens. The expansion of CompDam's capability to include matrix and delamination fatigue crack growth was identified as a technical development need for the project.

The CompDam material model represents matrix cracks as cohesive planes embedded in a volume of unidirectional fiber-reinforced material. The local deformation gradient tensor is scaled by the characteristic dimensions of the material point and decomposed into a cohesive displacement jump and a bulk material deformation gradient tensor [5]. The deformation decomposition is performed so as to maintain equilibrium across the inserted cohesive plane. The constitutive response of the bulk material is generally linear-elastic orthotropic, though pre-peak nonlinearity can be activated. The constitutive response of the embedded cohesive plane is a conventional mixed-mode linear-softening traction-separation law.

CompDam is implemented as a VUMAT user material subroutine for use with Abaqus/Explicit [6]. The material model can represent either individual fiber-reinforced plies when used with three-dimensional solid elements or interlaminar interfaces when used with cohesive elements. The same cohesive law logic is used for both intralaminar matrix cracks and interlaminar delaminations. As such, the integration of fatigue capability into the material model cohesive law would enable the modeling of matrix cracks, delaminations, and their interactions.

A novel cohesive fatigue model developed by Dávila [7] is based on engineering approximations of the endurance limit and the Goodman diagram. The method requires specification of only the typical strength and fracture toughness material properties for cohesive traction-separation laws and information concerning the stress-life behavior of the material. The stress-life behavior of the material is characterized by the endurance limit, ϵ, and the number of fatigue

*Research Aerospace Engineer, Durability, Damage Tolerance, and Reliability Branch, Mail Stop 188E
†Senior Research Aerospace Engineer, Durability, Damage Tolerance, and Reliability Branch, Mail Stop 188E, AIAA Member

cycles to the endurance, γ. With these inputs corrected for mode mixity and stress ratio, the method is capable of predicting the Paris law regime, as well as the transient effects of crack initiation and stable tearing, for a variety of fatigue loading conditions. The model was initially developed for implicit analyses and was implemented as a UMAT user material subroutine for cohesive elements with Abaqus/Standard.

In the cohesive fatigue model, the cohesive damage variable evolves as a function of fatigue cycles, with the rate depending on the current displacement jump. An empirical two-parameter function for incremental fatigue damage as a function of fatigue cycles was proposed in Ref. [7]. Additional definitions for the incremental fatigue damage function are proposed and evaluated in Ref. [8]. The evaluations included test/analysis correlations for double cantilever beam (DCB) and mixed-mode bending fracture characterization specimens and three-point bend (3PB) doubler validation specimens from ACP. Of the evaluated incremental fatigue damage functions, the four-parameter CF20 function had the most success in matching experimentally observed behaviors while requiring a minimal amount of experimental data.

In this extended abstract, Dávila's CF20 cohesive fatigue law is integrated into the CompDam material model. Analyses that take advantage of the scalability of explicit FE solvers are conducted, including size effect studies and larger structures that are computationally intractable with the implicit implementation. The abstract is organized as follows. Section II presents the integration of the cohesive fatigue model into an explicit constitutive material model. Section III includes a verification of the proper functioning of the explicit fatigue model in terms of cohesive traction-separation laws and stress-life behavior. Section IV includes a validation of the explicit implementation in which double cantilever beam (DCB) and three-point bend (3PB) doubler specimens are analyzed. Section V presents a parametric 3PB doubler analysis matrix in which specimen width is increased from 1/16-scale to full-scale, following the approaches laid-out in Refs. [9, 10]. The full paper will include FE analyses on size effects of the 3PB doubler problem in terms of crack growth rate and the conditions along the fatigue crack front. Discussions on the computational scalability of the implicit and explicit cohesive fatigue model implementations will also be included.

II. Cohesive Material Model

A. Quasi-Static Loading

The constitutive response of the cohesive law is a linear-softening traction-separation law:

$$\sigma = \begin{cases} K_n(1-d)\delta_n, & \text{if } \delta_n \geq 0 \\ K_n\delta_n, & \text{otherwise} \end{cases} \tag{1}$$

$$\tau = K_s(1-d)\delta_s \tag{2}$$

where σ is the normal traction, τ is the shear traction, the δ terms represent the cohesive displacement jumps, the K terms represent the numerical penalty stiffness, and d is a scalar damage state variable, Fig. 1. The subscripts n and s represent the crack normal and shear directions. The Mode I and Mode II strength and fracture toughness properties are σ_c, τ_c, $G_{\mathrm{I}c}$, and $G_{\mathrm{II}c}$, respectively.

Damage initiates when the current cohesive displacement jump, δ, reaches the failure initiation displacement jump, δ_0. After damage initiation, the damage state variable evolves from zero (representing an undamaged state) to one (representing a fully damaged state). Damage is fully developed when δ reaches the final failure displacement jump δ_f.

The current damage variable, d, is a function of the current displacement jump, δ, and δ_0 and δ_f:

$$d = \frac{\delta_f(\delta - \delta_0)}{\delta(\delta_f - \delta_0)} \tag{3}$$

An alternative damage variable can be expressed in terms of normalized fracture energy dissipation with the form:

$$\bar{d} = \frac{d\delta_0}{(1-d)\delta_f + d\delta_0} \tag{4}$$

which has the benefit of being independent of the penalty stiffness.

The displacement jump values for damage initiation and final failure are functions of the strength and fracture toughness material properties, the penalty stiffness terms, and the mode mixity, B, following the derivation in Ref. [11]. Mode mixity is defined according to the Mode II energy release rate over the total energy release rate through:

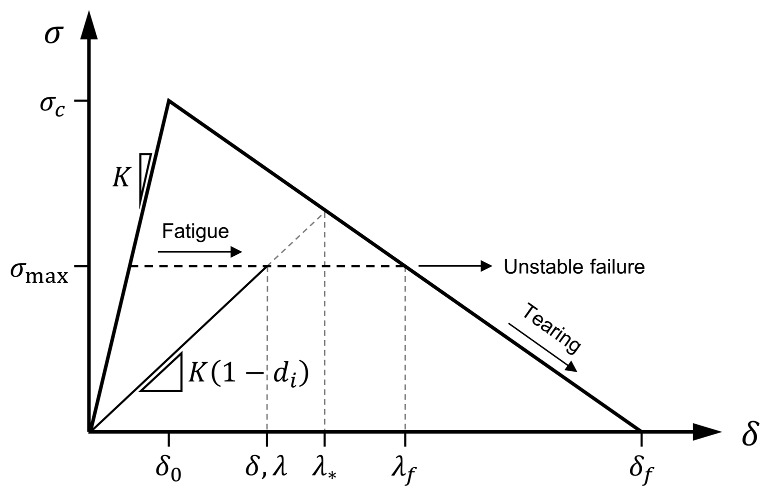

Fig. 1 Cohesive fatigue traction-separation law for constant-traction fatigue growth.

$$B = \begin{cases} \frac{K_s \delta_s^2}{K_s \delta_s^2 + K_n \delta_n^2}, & \text{if } \delta_n > 0 \\ 1, & \text{otherwise} \end{cases} \tag{5}$$

For pure normal and shear loading conditions, the initiation displacement jumps are:

$$\begin{aligned} \delta_{0n} &= \frac{\sigma_c}{K_n} \\ \delta_{0s} &= \frac{\tau_c}{K_s} \end{aligned} \tag{6}$$

and the final failure displacement jumps are:

$$\begin{aligned} \delta_{fn} &= \frac{2G_{\mathrm{I}c}}{\sigma_c} \\ \delta_{fs} &= \frac{2G_{\mathrm{II}c}}{\tau_c} \end{aligned} \tag{7}$$

Under mixed-mode loading conditions where $0 < B < 1$, the cohesive response is defined according the Benzeggagh-Kenane (BK) law [12]. The mixed-mode initiation displacement jump δ_0 is:

$$\delta_0 = \sqrt{\left(\delta_{0n}^2 + (\delta_{0s}^2 \frac{K_s}{K_n} - \delta_{0n}^2) B^{\eta_{\mathrm{BK}}}\right)\left(1 + B(\frac{K_n}{K_s} - 1)\right)} \tag{8}$$

and the mixed-mode final failure displacement jump δ_f is:

$$\delta_f = \frac{1}{\delta_0}\left(\delta_{0n}\delta_{fn} + (\delta_{0s}\delta_{fs}\frac{K_s}{K_n} - \delta_{0n}\delta_{fn})B^{\eta_{\mathrm{BK}}}\right)\left(1 + B(\frac{K_n}{K_s} - 1)\right) \tag{9}$$

where η_{BK} is the exponent of the BK fracture criterion.

B. Fatigue Loading

The CF20 incremental fatigue damage function requires information regarding the endurance limit ϵ and the fatigue cycles to endurance γ. ϵ is the endurance limit for fully reversed ($R = -1$) axial loading. Shear loading representative of Mode II and mixed-mode loading conditions can be accounted for in the endurance limit through:

$$\epsilon_{\mathrm{mixed}} = \epsilon(1 - 0.42B), \tag{10}$$

and different stress ratios, R, can be accounted for with the correction:

Table 1 CF20 cohesive fatigue model inputs

Parameter	Description	Value
γ	Number of fatigue cycles to reach endurance	1×10^7
ϵ	Endurance limit	0.2
η	Brittleness	0.95
p	Curve-fitting parameter to match Paris Law results	β

$$E = \frac{2\epsilon_{\text{mixed}}}{\epsilon_{\text{mixed}} + 1 + R(\epsilon_{\text{mixed}} - 1)}, \tag{11}$$

where E is referred to as the relative endurance limit.

The CF20 incremental fatigue damage function is written in terms of normalized energy dissipation and has the assumed shape:

$$\Delta \bar{d}_{\text{fat}} = \frac{1}{\gamma} \frac{(1 - \bar{d}_{i-1})^{\beta - p}}{E^{\beta}(p + 1)} (\frac{\lambda}{\lambda_*})^{\beta} \Delta N_i \tag{12}$$

where the subscript i represents the current solution increment and ΔN_i is the number of fatigue cycles represented by the current solution increment. λ is the peak displacement jump within a fatigue cycle, and λ_* is the displacement jump at which static damage progression would occur given the current mode mixity and prior damage state, as shown in Fig. 1. The ratio $\frac{\lambda}{\lambda_*}$ is referred to as the relative displacement jump, and can be expressed as:

$$\frac{\lambda}{\lambda_*} = \frac{\delta_i}{(1 - \bar{d}_{i-1})\delta_0 + \bar{d}_{i-1}\delta_f} \tag{13}$$

β is a function of E and a "brittleness" input parameter η:

$$\beta = \frac{-7\eta}{\log E} \tag{14}$$

p is an additional parameter from the fatigue damage accumulation law of Allegri and Wisnom [13] that affects the predicted pre-factor of the Paris law. In total, the incremental fatigue damage function in Eq. 12 has four input parameters, which are listed in Table 1 along with their values used in the analyses presented in this paper.

The current damage state is the sum of the previous damage state and current incremental fatigue damage:

$$\bar{d}_i = \bar{d}_{i-1} + \Delta \bar{d}_{\text{fat}} \tag{15}$$

Converting from the normalized energy dissipation form to the cohesive damage state variable form for compatibility with the rest of the material model logic yields:

$$d_i = \frac{\delta_f \bar{d}_i}{\delta_0(1 - \bar{d}_i) + \delta_f \bar{d}_i} \tag{16}$$

If damage evolution occurs due to both static and fatigue loading, the maximum of the current static and current fatigue damage states is used.

C. Representation of Fatigue Cycles

The cohesive fatigue model simulates the accumulation of fatigue damage via simplified cyclic loading (SCL) in which either maximum applied loads or displacements are held constant while fatigue cycles pass with step time. A fatigue analysis with SCL requires at least two analysis steps. In the first step(s), the structure is quasi-statically loaded to the peak of a fatigue cycle. Then, in the following fatigue analysis step, the applied loads or displacements are held constant while fatigue damage accumulates.

In the implicit implementation of the cohesive fatigue model, the analysis pseudo-time represents fatigue cycles [7]. In an implicit analysis, the time increment, Δt, automatically increases or decreases as necessary to reach converged

Table 2 User-defined solution parameters controlling the evolution of ΔN_i

Parameter	Description	Default Value
$(\Delta N_i)_{\text{initial}}$	fatigue cycles per increment, initial	1×10^{-4}
$(\Delta N_i)_{\text{max}}$	fatigue cycles per increment, max.	1×10^{5}
$(\Delta N_i)_{\text{min}}$	fatigue cycles per increment, min.	1×10^{-5}
$(\Delta N_i)_{\text{mod}}$	percent change modifier of ΔN_i	1×10^{-1}
$(\Delta \bar{d}_{\text{fat}})_{\text{max}}$	incremental energy dissipation, max.	1×10^{-4}
$(\Delta \bar{d}_{\text{fat}})_{\text{min}}$	incremental energy dissipation, min.	5×10^{-6}

solutions while the fatigue damage accumulates, using smaller time increments when damage growth is rapid and larger time increments when damage growth is slow. During an explicit analysis step, the time increment is capped at the minimum stable time increment, Δt_{stable}. The total number of solution increments is also limited by the eventual accumulation of significant numerical error. These two limits on the time incrementation must be considered while designing the representation of fatigue cycles in the explicit analysis steps. Three options were considered with regard to how to represent the fatigue cycles in an explicit analysis step, starting with the approach adopted in the implicit implementation:

1) **Constant fatigue cycles per delta time**, $\Delta N/\Delta t = c_1$
This is the approach used in the implicit implementation, and would be simple to implement. Negative factors associated with this approach include the possibility that Δt_{stable} can change during the fatigue analysis step due to either fatigue damage accumulation or other nonlinear effects. Because the explicit solver cannot raise the time increment above Δt_{stable}, the solution cannot advance more quickly when damage growth is slow and inefficiently spends many solution increments modeling periods of slow damage growth. In addition, the selection of the constant value c_1 requires a good estimate of the fatigue life before performing the analysis.
2) **Constant fatigue cycles per solution increment**, $\Delta N_i = c_2$
Making fatigue cycles depend on the solution increment, Δi, rather than Δt allows fatigue damage to accumulate independent of Δt_{stable}. However, a linear distribution of solution increments over the fatigue cycle history in maintained. A constant ratio of fatigue cycles per solution increment requires an analyst to compromise between using too few increments during periods of rapid damage growth and not reaching the fatigue life before numerical errors accumulate to unacceptable levels. Again, a good estimate of the fatigue life would be needed to select a value for c_2 that may produce acceptable results.
3) **Variable fatigue cycles per solution increment**, $\Delta N_i = f(\cdot)$
Allowing the ratio of fatigue cycles per solution increment to change during the analysis addresses the concerns of the prior two options: it avoids coarse representation of rapid changes in damage states; fewer increments are wasted modeling periods of slow damage growth; the model can adapt to the current damage accumulation rate; and *a priori* knowledge of the fatigue life is not required. A negative factor with this option is its relative complexity, requiring that a procedure, $f(\cdot)$, is developed that allows ΔN_i to change as needed.

In order to allow for computationally efficient fatigue analyses without *a priori* knowledge of the fatigue life, a numerical procedure was developed to define ΔN_i as a function of $\Delta \bar{d}_{\text{fat}}$ Eq. 12). Several user-defined parameters are used to control the evolution of ΔN_i during the analysis, each of which are listed and defined in Table 2 and illustrated in Fig. 2. The parameter $(\Delta N_i)_{\text{initial}}$ defines the initial ratio of fatigue cycles per solution increment. At each material point and during every solution increment, $\Delta \bar{d}_{\text{fat}}$ is calculated. At the end of each solution increment, if the maximum value of $\Delta \bar{d}_{\text{fat}}$ for all material points is outside the bounds set by $(\Delta \bar{d}_{\text{fat}})_{\text{min}}$ and $(\Delta \bar{d}_{\text{fat}})_{\text{max}}$, ΔN_i is adjusted for the next solution increment. If fatigue damage is progressing too slowly with respect to solution increments, ΔN_i is multiplied by $(1 + (\Delta N_i)_{\text{mod}})$, up to a maximum value of $(\Delta N_i)_{\text{max}}$. If, instead, fatigue damage is progressing too rapidly, ΔN_i is divided by $(1 + (\Delta N_i)_{\text{mod}})$, down to a minimum value of $(\Delta N_i)_{\text{min}}$.

At the beginning of a fatigue analysis step, ΔN_i typically increases after every increment until either damage is progressing by $(\Delta \bar{d}_{\text{fat}})_{\text{min}}$ somewhere in the model or $(\Delta N_i)_{\text{max}}$ is reached. During this period (shaded green in Fig. 2), ΔN and N are functions of i and the solution parameters:

$$\Delta N(i) = (\Delta N_i)_{\text{initial}} \left[1 + (\Delta N_i)_{\text{mod}}\right]^{i-1} \tag{17}$$

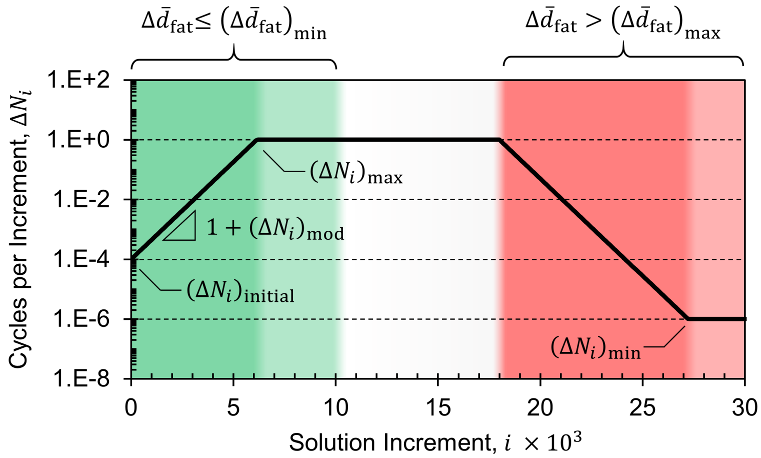

Fig. 2 Solution parameters controlling the evolution of ΔN_i.

$$N(i) = \frac{(\Delta N_i)_{\mathrm{initial}}}{(\Delta N_i)_{\mathrm{mod}}}\left([1 + (\Delta N_i)_{\mathrm{mod}}]^i - 1\right) \tag{18}$$

These functions for $\Delta N(i)$ and $N(i)$ can be used to select solution parameters that will, for example, achieve a certain ratio of fatigue cycles per solution increment after a certain number of solution increments.

III. Verification

Single-element FE verification analyses were run for pure Mode I and pure Mode II loading conditions. The objective of these single-element analyses is to verify that the shapes of constitutive traction-separation laws and the stress-life plots replicate their designed, intended behaviors. The elements have in-plane dimensions of 0.1 mm in the x and y directions and zero initial thickness in the z direction. The nominal IM7/8552 interlaminar properties from Table 3 are used. Two analysis steps are used in each analysis. The first analysis step includes the quasi-static application of equal loads to the four $+z$-surface nodes of the cohesive element, in the $+z$ direction for axial loading and in the $+x$ direction for shear loading. The displacements of $+z$ nodes are constrained in the unloaded directions, and the $-z$ nodes are fixed in all three directions. During the second analysis step, load is held constant while fatigue damage accumulates. The verification analyses are performed using the Abaqus/Explicit 2019 solver with double precision. Geometric nonlinearity is enabled in all analysis steps. Mass scaling is applied so as to maintain $\Delta t_{\mathrm{stable}} > 1 \times 10^{-7}$ seconds at all increments.

Traction-displacement histories for six analyses are shown in Fig. 3, including static loading, fatigue loading with $\sigma_{\mathrm{max}}/\sigma_c = 0.5$, and fatigue loading with $\sigma_{\mathrm{max}}/\sigma_c = 0.8$ for both normal and shear loading conditions. The model traction-displacement histories match the designed behavior of maintaining constant traction during damage evolution until the static unloading curve is reached. When the static unloading curve of the cohesive law is reached, the material can no longer sustain the applied maximum load and dynamic failure occurs. Although the applied maximum load remains constant during failure, dynamic reaction forces develop that counteract the applied load such that the net load follows the unloading curve, as shown in Fig. 3.

Single-element, constant-maximum-stress analyses were performed for four different values of R (−1, 0, 0.1, and 0.5) to evaluate the models' ability to reproduce the corresponding stress-life diagrams. For each R, analyses were performed with several values of the fatigue strength $\sigma_{\mathrm{max}}/\sigma_c$, starting at 0.99 and decreasing until the predicted fatigue life exceeded the endurance limit of 1×10^7 cycles. The resulting strength-life plots are shown in Fig. 4. The analysis results (black and white open symbols) match very well the behavior described by the fatigue life equations (black solid and dashed lines).

Table 3 IM7/8552 interface material properties for use with a single (nominal) layer and with two superposed (initiation + bridge) layers of cohesive elements [7]

Property	Units	Nominal	Initiation	Bridge
σ_c	MPa	80.1	80.0	0.8
τ_c	MPa	97.6	99.0	1.0
G_{Ic}	N-mm/mm^2	0.240	0.214	0.140
G_{IIc}	N-mm/mm^2	0.739	0.59	0.193
η_{BK}	-	2.1	2.1	3.0
K_n	MPa/mm	200,000	200,000	2,000

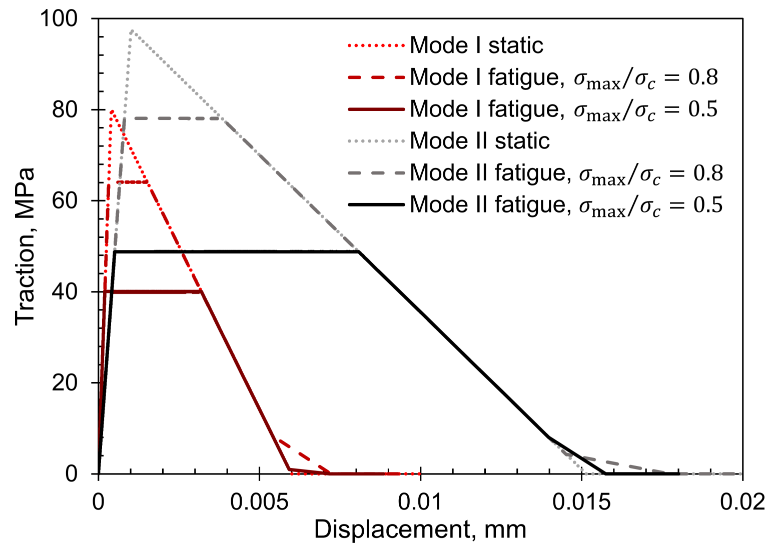

Fig. 3 Traction-displacement histories of single-element verification analyses.

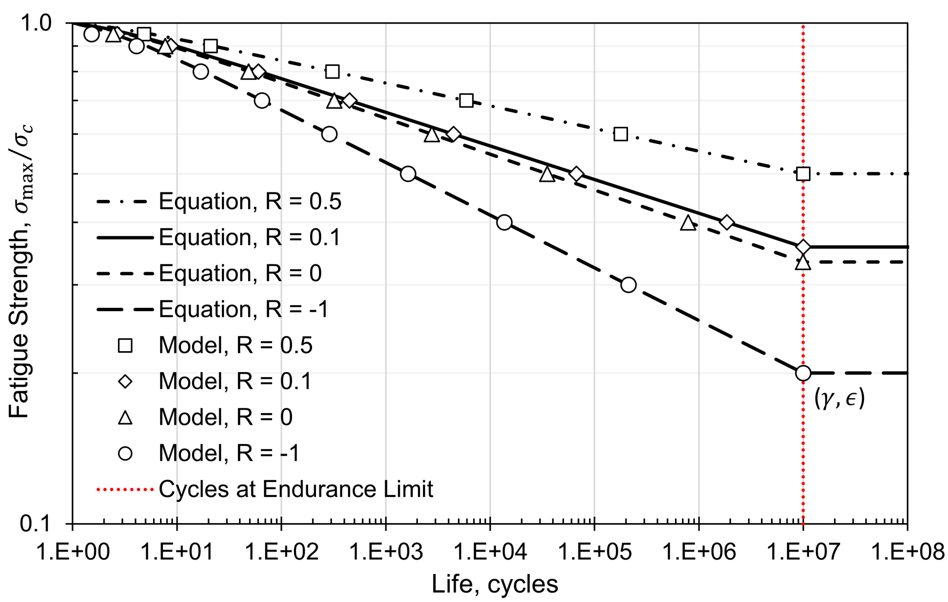

Fig. 4 Strength-life plots from single-element verification analyses for Mode I loading, compared to the fatigue life equations on which the code is based.

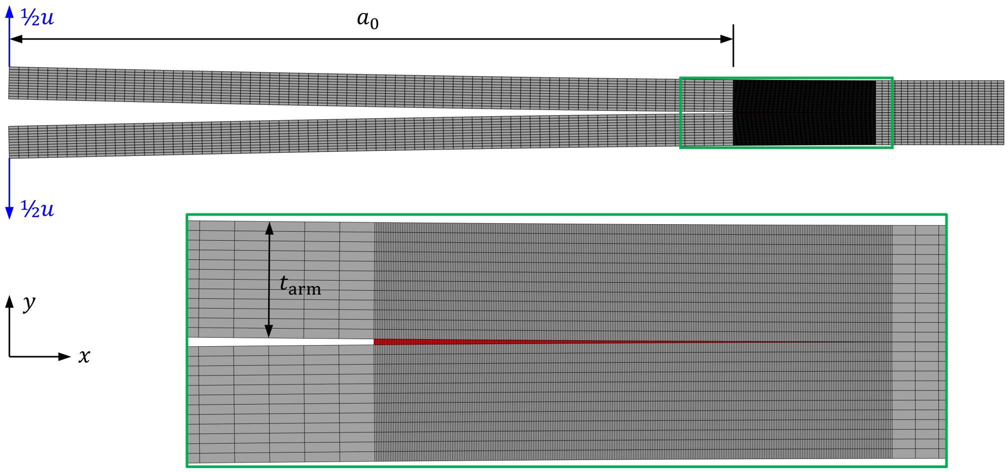

Fig. 5 DCB finite element model.

Table 4 IM7/8552 unidirectional tape material properties

Property	Units	Value
E_1	MPa	146,671
E_2	MPa	8703
E_3	MPa	8703
ν_{12}	-	0.32
ν_{13}	-	0.32
ν_{23}	-	0.45
G_{12}	MPa	5164
G_{13}	MPa	5164
G_{23}	MPa	3001

IV. Validation

A. Doubler Cantilever Beam

Analyses of double cantilever beam (DCB) specimens subjected to cyclic fatigue loading under displacement control are used to validate the concept of the cohesive fatigue model and its implementation within an explicit FE material model. The geometry and conditions of this example problem correspond to the DCB configuration presented in Refs. [7, 8]. The models are composed of unidirectional IM7/8552 carbon/epoxy tape, with pertinent intralaminar material properties listed in Table 4. An initial crack length, a_0, of 50.8 mm is assumed, and the loading arms have a thickness, t_{arm}, equal to 2.25 mm. Twelve layers of CPE4R reduced-integration plane strain elements represent each loading arm. A plane strain width, w, of 25.4 mm is used. The interface is modeled with two superposed layers of two-dimensional, four-node COH2D4 cohesive elements. The two superposed layers of cohesive elements are used to represent an experimentally observed R-curve response in which noticeable fiber bridging occurs. The two superposed layers of cohesive elements use the "Initiation" and "Bridge" interlaminar material properties listed in Table 3, respectively. Global and crack tip views of the model are shown in Fig. 5.

In the experimental work of Murri [14], four different values of maximum applied displacements, u, were used: 1.48, 1.70, 1.92, and 2.25 mm. Explicit fatigue analyses for each of these four applied displacement values were conducted. The load and fatigue cycle histories allow for the calculation of the specimen compliance, crack length, a, and energy release rate, $G_{\text{I,max}}$, following the approach of Reeder et al. [15]. The predicted rates of crack propagation, da/dN, for each of the maximum applied displacements are shown in Fig. 6 for the explicit analyses, the experiments, and the implicit analyses. The explicit analysis results (solid lines) match the implicit results (dashed lines) and the experimental data for all applied displacement values.

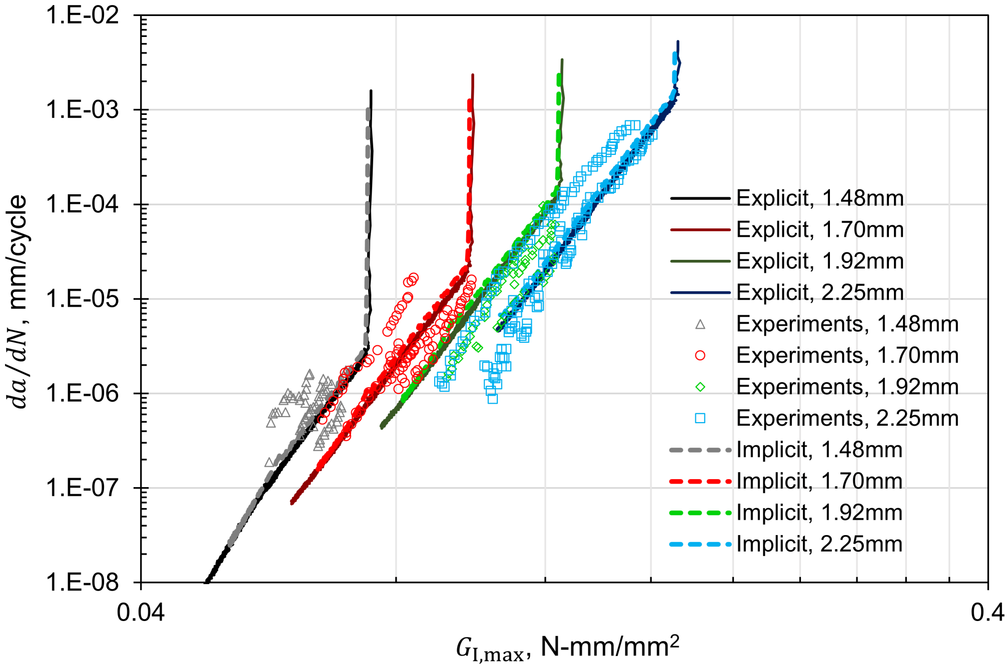

Fig. 6 da/dN **versus** $G_{\mathrm{I,max}}$ **for DCB explicit analyses, experiments, and implicit analyses for different peak applied displacements.**

B. Three-Point Bend Doubler

Analyses of 3PB specimens with a central doubler are performed to validate the implementation of the cohesive fatigue law in the explicit material model for mixed-mode loading conditions. In addition, the 3PB doubler model configuration is used to demonstrate the computational scalability of the explicit implementation while studying structural size effects.

The deformed mesh of the 3PB doubler FE model is shown in Fig. 7. The specimen skin (light blue) is composed of IM7/8552 tape. The skin is modeled with three layers of SC8R continuum shell elements, has a stacking sequence of $[+45/-45/0/90/+45/-45]_S$, and a thickness t_{skin} of 2.20 mm. The doubler (green) is composed of AS4/8552 plain-weave fabric (Table 5) and has a length L_{doubler} of 101.6 mm. The doubler is modeled with two layers of SC8R continuum shell elements. The stacking sequence of the doubler is $[+45/-45/0/+45_2/0/-45/+45_2/-45/0/+45]$, and it has a thickness, t_{doubler}, of 2.38 mm. A reduced model width, w, of 3.175 mm is used to reduce the computational cost of the model to allow for comparisons of the implicit and explicit predictions.

The interface between the doubler and the skin panel is modeled with two superposed layers of three-dimensional, eight-node COH3D8 cohesive elements to represent an experimentally observed R-curve response [16]. The two superposed layers of cohesive elements use the "Initiation" and "Bridge" interlaminar material properties listed in Table 6, respectively.

Fatigue tests were conducted for the 3PB doubler specimens under load control for three fatigue cycle peak loads: 214 N, 167 N, and 155 N. Two cylindrical, 50.8-mm-diameter rollers and a single, central 12.7-mm-diameter roller were used to load the specimens. The spacing of the two outer rollers, L_{loaders}, was 203.2 mm.

Results in terms of delamination length, Δa, versus fatigue cycles, N, are presented in Fig. 8 for experimental results, implicit analyses, and explicit analyses. Crack growth rates at either side of the doubler are not equal due to a small numerical asymmetry intentionally applied to the model. Results are presented for crack growth from the left and right sides of the doubler (as pictured in Fig. 7). Good agreement between the experimental results and the implicit predictions were previously demonstrated in Ref. [8], and similar results are reproduced here. In addition, the explicit Δa versus N results match closely the implicit predictions for all three peak applied load values and throughout the fatigue histories.

Table 5 IM7/8552 plain-weave fabric material properties

Property	Units	Value
E_1	MPa	66,000
E_2	MPa	65,800
ν_{12}	-	0.052
G_{12}	MPa	5100
G_{13}	MPa	3400
G_{23}	MPa	3400

Table 6 Tape/fabric interlaminar material properties for the 3PB analyses

Property	Units	Initiation	Bridge
σ_c	MPa	105.0	4.0
τ_c	MPa	90.0	12.0
$G_{\mathrm{I}c}$	N-mm/mm^2	0.35	0.60
$G_{\mathrm{II}c}$	N-mm/mm^2	1.0	3.5
η_{BK}	-	2.07	3.0
K_n	MPa/mm	500,000	19,048

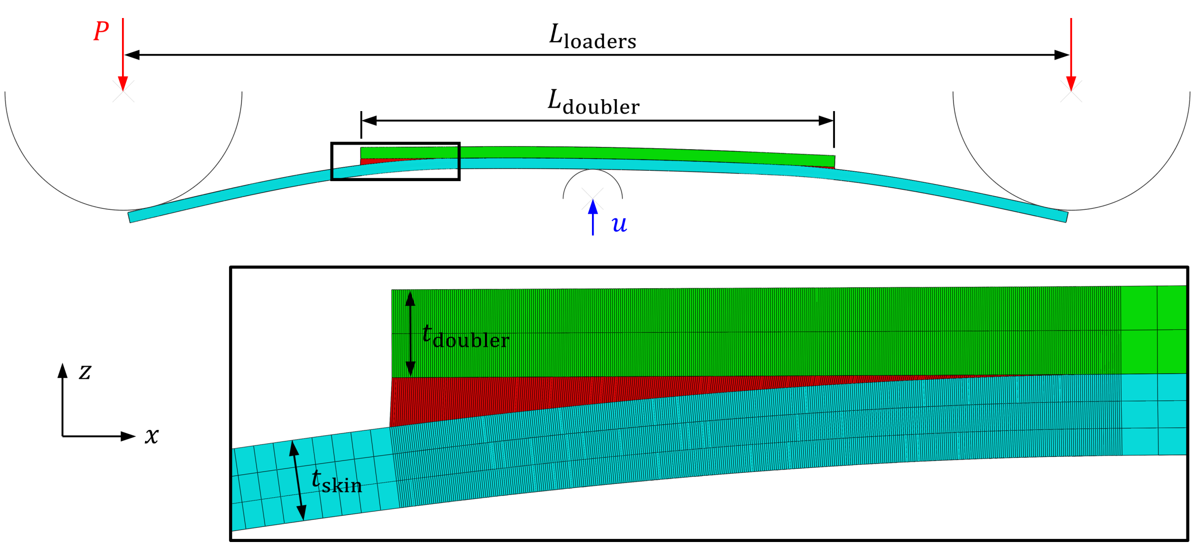

Fig. 7 3PB doubler FE model, shown in its deformed state at the end of the fatigue analysis step.

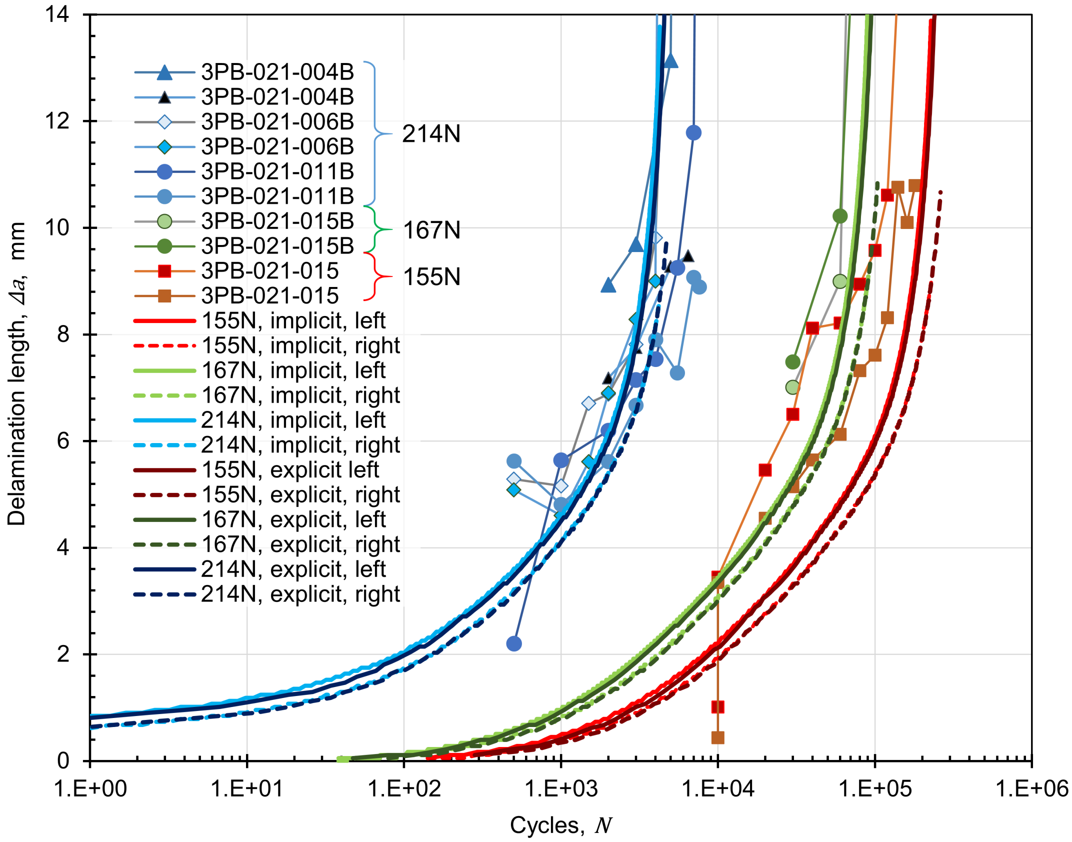

Fig. 8 Crack extension Δa versus fatigue cycles N for the 3PB doubler tests and analyses at three different fatigue cycle peak loads: 214 N (blue), 167 N (green), and 155 N (red).

V. Scalability

In the full paper, computational scalability studies will be presented using the 3PB doubler fatigue model. The width of the FE model will be incrementally increased from the reduced 1/16-scale presented in Section IV.B to full scale while maintaining all other model parameters, e.g., element size across the width, solution time increment size. Explicit analyses will be conducted with a set number of CPUs, and scalability will be reported in terms of wallclock time versus degrees of freedom. Implicit analyses will also be performed for the increased widths, though only up to the point where model run times become qualitatively impractical. Analysis results will be compared in terms of crack length versus fatigue cycles, fatigue crack front shape, and the mode-mix composition of the crack front.

The results of the 3PB doubler scalability study will be used to estimate the ability of the explicit implementation of the cohesive fatigue model to analyze larger structural problems, including the seven-point bending and single stringer compression specimens tested as part of the NASA ACP. The static analyses of these structures involved ply-by-ply meshing of the problem so as to predict the initiation, growth, and interaction of discrete matrix cracks and delaminations on multiple interfaces [3, 4]. The computational tractability assessment will be for the same multi-interface conditions and FE meshes used in the previous static analysis studies.

References

[1] Wanthal, S., Schaefer, J., Justusson, B., Hyder, I., Engelstad, S., and Rose, C., "Verification and Validation Process for Progressive Damage and Failure Analysis Methods in the NASA Advanced Composites Consortium," *32nd American Society for Composites Technical Conference*, West Lafayette, IN, 2017.

[2] Leone, F. A., Bergan, A. C., and Dávila, C. G., "CompDam - Deformation Gradient Decomposition (DGD), v2.5.0," , 2019. https://github.com/nasa/CompDam_DGD.

[3] Leone, F. A., Song, K., Johnston, W., Rose, C. A., Jackson, W. C., and Dávila, C. G., "Test/Analysis Correlation of Damage States in Post-buckled Stiffened Validation Building Block Specimens," *34th American Society for Composites Technical Conference*, Atlanta, GA, 2019.

[4] Leone, F. A., Song, K., Rose, C. A., and Jackson, W. C., "Progressive Damage Analysis of Post-Buckled Stiffened Panels under Static Compressive Loading," *AIAA SciTech Forum*, Orlando, FL, 2020.

[5] Leone, F. A., "Deformation Gradient Tensor Decomposition for Representing Matrix Cracks in Fiber-Reinforced Materials," *Composites Part A: Applied Science and Manufacturing*, Vol. 76, 2015, pp. 334–341. https://doi.org/10.1016/j.compositesa.2015.06.014.

[6] ABAQUS, *Abaqus 6.19 Online Documentation*, Dassault Systèmes, Providence, RI, 2019.

[7] Dávila, C. G., "From S-N to the Paris Law with a New Mixed-Mode Cohesive Fatigue Model," NASA/TP-2018-219838, NASA Langley Research Center, Hampton, Va., Dec. 2018.

[8] Dávila, C. G., Rose, C. A., Jackson, W. C., and Johnston, W., "Evaluation of Fatigue Damage Accumulation Functions for Delamination Initiation and Propagation," NASA/TP-2020-220584, NASA Langley Research Center, Hampton, Va., Apr. 2020.

[9] Bergan, A. C., "Computational Performance of Progressive Damage Analysis of Composite Laminates using Abaqus/Explicit with 16 to 512 CPU Cores," NASA/TM-2019-220251, NASA Langley Research Center, Hampton, Va., Feb. 2019.

[10] Bergan, A. C., Leone, F. A., Boyd, S., Hyder, I., and Schaefer, J. D., "Computational Considerations in Scaling the Application of Progressive Damage Analysis Methods from Coupons to Sub-Components," *34th American Society for Composites Technical Conference*, Atlanta, GA, 2019.

[11] González, E. V., Maimí, P., Turon, A., Camanho, P. P., and Renart, J., "Simulation of Delamination by Means of Cohesive Elements Using an Explicit Finite Element Code," *Computers, Materials & Continua*, Vol. 9, No. 1, 2009, pp. 52–92. https://doi.org/10.3970/cmc.2009.009.051.

[12] Benzeggagh, M. L., and Kenane, M., "Measurement of Mixed-Mode Delamination Fracture Toughness of Unidirectional Glass/Epoxy Composites with Mixed-Mode Bending Apparatus," *Composites Science and Technology*, Vol. 56, 1996, pp. 439–449.

[13] Allegri, G., and Wisnom, M. R., "A Non-linear Damage Evolution Model for Mode II Fatigue Delamination Onset and Growth," *International Journal of Fatigue*, Vol. 43, 2012, pp. 226–234. https://doi.org/10.1016/j.ijfatigue.2012.03.016.

[14] Murri, G. B., "Evaluation of Delamination Onset and Growth Characterization Methods under Mode I Fatigue Loading," NASA/TP-2013-217966, NASA Langley Research Center, Hampton, Va., Feb. 2013.

[15] Reeder, J. R., Demarco, K., and Whitley, K. S., "The Use of Doubler Reinforcement in Delamination Toughness Testing," *Composites: Part A*, Vol. 35, 2004, pp. 1337–1344. https://doi.org/10.1016/j.compositesa.2004.02.021.

[16] Dávila, C. G., Leone, F. A., Song, K., Ratcliffe, J. G., and Rose, C. A., "Material Characterization for the Analysis of Skin/Stiffener Separation," *32nd American Society for Composites Technical Conference*, West Lafayette, IN, 2017.